JOURNAL OF MATERIALS SCIENCE 25 (1990) 1724–1738

Early stages of oxidation of yttrium-implanted Ni–20% Cr

C. H. YANG*, G. WELSCH, T. E. MITCHELL‡
Department of Materials Science and Engineering, Case Western Reserve University, 10900 Euclid Avenue, Cleveland, Ohio 44106, USA

The effect of ion-implanted yttrium on oxidation at elevated temperatures (500 to 1000° C) has been studied in Ni–Cr alloys using high-voltage electron microscopy (HVEM) of *in situ* oxidized specimens, electron microscopy of scales oxidized *ex situ*, and Rutherford back scattering. The presence of yttrium enhances nucleation and growth of Cr_2O_3 at the alloy surface. Although the radiation damage induced by the ion implantation accelerates oxide nucleation and the initial rate of oxidation at 500° C, the growth of a mature oxide scale is slowed down, and the main influences seem to come from the chemical characteristics of the implanted yttrium. A Cr_2O_3 layer forms first on the yttrium-implanted alloys. Outward diffusion of Ni^{2+} cations through this layer forms an outer NiO scale. The initial growth process on unimplanted alloys is opposite. Here, NiO is the predominant initial oxide. As it thickens, a porous spinel and Cr_2O_3-enriched layer is formed between alloy and NiO. The inner oxide layer on yttrium-implanted alloys is fully dense and contains more than 50% Cr_2O_3. On the unimplanted alloy, the inner spinel layer is porous and contains a lesser enrichment in Cr_2O_3. The porous spinel delays formation of a protective Cr_2O_3 layer and gives poor scale adherence. The oxide growth mechanisms are discussed in the light of TEM results.

1. Introduction

The beneficial effects of reactive elements on the oxidation behaviour of alloys are well known [1, 2]. In particular, the oxidation resistance of chromium-containing alloys is improved by the addition of small amounts of yttrium [2]. Previous investigations on Ni–Cr alloys [3] have shown that the oxide growth rate is decreased by a factor of two by yttrium addition. The rare earth effect is even more prominent for lanthanum to niobium-stabilized 20% Ni–25% Cr stainless steel [4, 5]. The scale adherence is indicated by oxide spallation during thermal cycling; on undoped 20/25/Nb stainless steel, up to 80% of the oxide spalled. Lanthanum-doping improved oxide adhesion, and no spallation was measurable.

The objective of the present work was a microstructural investigation of the nucleation and early growth of oxide on Ni–Cr alloys. It was of particular interest to explore how ion-implanted yttrium affects the nucleation and growth of the oxide scale, and to gain more insight into the mechanisms by which yttrium reduces the oxide growth rate and enhances the oxide scale adherence at the same time.

The reactive element effect has been investigated with a number of analytical techniques, including electron microprobe analysis (EMPA), secondary ion mass spectroscopy (SIMS), and Rutherford back scattering (RBS) [3, 4] in order to identify the scale structure and location of the reactive elements. Recent examination by analytical electron microscopy (AEM) of transverse sections through the oxide scale has revealed the full scale structure in 20/25/Nb stainless steel [5] and in Ni–Cr alloys [6]. On Ni–20% Cr, the mature scale consists of multiple oxide layers: $NiO/NiCr_2O_4/Cr_2O_3$/alloy. Even though there have been many efforts to comprehend the reactive element effect on oxidation kinetics and on the structure and morphology of the oxide scale, the mechanisms are still unclear. Ion-implantation is a convenient method of homogeneously doping the surface layer with reactive elements, and despite the shallowness of the implant depth (less than 0.5 μm), it has been shown to exert its effect even in long-term oxidation experiments in which scales of several micrometres thickness grow [7]. Besides the change in chemistry, ion implantation also introduces lattice defects and therefore an additional physical factor which may influence the nucleation and initial growth of oxide.

The early stages of scale development have received little study. It is known that after exposure for as little as 10 min at 1000° C [8] a multiple oxide scale develops on Ni–20% Cr. In the present study we have used RBS and TEM examination on oxide particles and scales developed after 1 to 5 min in order to understand the influence of yttrium on the initial nucleation and growth of the scale on Ni–Cr alloys.

Present address: IBM Corporation, East Fishkill, New York 12533, USA.
‡*Present address*: Los Alamos National Laboratory, Los Alamos, New Mexico 87545, USA.

0022-2461/90 $03.00 + .12

2. Experimental techniques

The composition and preparation of Ni–20% Cr alloys has been reported in a previous paper [6]. The ion implantation was performed at 280 kV to a dose of 2×10^{16} Y ion cm^{-2}. Discs of 3 mm diameter were punched from annealed, polished strips of implanted and unimplanted Ni–20% Cr alloys. The discs were then jet-polished electrolytically in a solution of 95% glacial acetic acid with 5% percholoric acid. The implanted specimens were jet-polished only on one side by protecting the implanted surface with lacquer.

In situ examination of the gas–metal reaction at elevated temperatures was performed in a Gatan environment cell and heating stage in the Argonne high-voltage electron microscope (Kratos/AE7 HVEM operating at 1 MeV). In the environmental cell, temperature was measured in a platinum ribbon heater which can reach above 1000° C in a few seconds, by monitoring the current passing through the heater. A furnace-type heater was also used in which the temperature was directly read from a thermocouple. The maximum temperature for oxidation was limited by the gas pressure in the cell. At $\sim 10^{-5}$ torr pressure, the maximum temperature was about 710° C, and it took 5 to 10 min to heat the specimens up to this temperature. The first 5 min oxidation could not be recorded because the sample drifted during the heating procedure.

Short-term oxidation was also carried out *ex situ* by inserting specimens into a heated quartz tube with 20 torr pure, dry flowing oxygen. The specimens were transported to and from the hot zone within 30 sec by means of a thin platinum boat in which the specimens could be quickly heated and cooled so that shorter oxidation times could be obtained. The oxidation time was counted from the point in time when a sample arrived at the hot zone. The samples were isothermally oxidized in the temperature range from 800 to 1000° C for periods of 1 to 5 min.

Ni–20% Cr and the yttrium-implanted Ni–20% Cr strips were cleaned ultrasonically in methanol for 5 min prior to oxidation. Samples for RBS were cut with a diamond saw in the form of small coupons, 2 mm × 5 mm × 550 μm thick. After the RBS analysis, 3 mm length strips were prepared from the same samples for TEM examination.

Rutherford back scattering analysis was performed on the Tandem accelerator at Argonne National Laboratory with 1.9 MeV He^{2+} ions. The scattering geometry was set for normal incidence and for a detecting angle of $\theta = 135°$, $\Omega = 4.1$ msr collection angle and a beam current of 15 μA. The basic concept of RBS and the experimental arrangement are described by Averback [9]. The interpretation of the RBS spectra and semiquantitative analysis have been performed in accordance with Chu *et al.*[10].

3. TEM results of *in situ* oxidation

Oxide nuclei were investigated by *in situ* oxidation in an HVEM environmental cell on yttrium-implanted and unimplanted Ni–20% Cr alloys in the temperature range 500 to 1000° C and at an oxygen pressure of 10 torr. Results were obtained on nucleation rate, crystal structure of nuclei, and orientation relationship between oxide nuclei and alloy substrate. Also the changes in the nuclei characteristics on increasing the temperature from 600 to 1000° C were examined.

3.1. Nucleation and early oxide growth on Ni–20% Cr alloy

Figure 1 shows fine oxide grains that nucleated both at grain boundaries and within the grains during oxidation at 600° C for several minutes. The high density of dislocations in the alloy, Fig. 1a, was already present before oxidation. The nucleation appears to be random and is not preferentially associated with dislocations or grain boundaries. However, the nucleation rate appeared higher near the edge of the TEM foil. The diffraction pattern (Fig. 1c) indicates that the first oxide is NiO. NiO is clearly revealed in the selected-area diffraction pattern by spotty diffraction rings. Very fine, randomly oriented NiO particles that have no particular orientation relationship to the alloy substrate give rise to the pattern. Because the rate of oxidation was relatively slow at 600° C the alloy diffraction spots remained prominent even after 15 min oxidation time. After 2 h oxidation, the foil edge was oxidized through. The oxide morphology is seen in Fig. 2. It consists of fine oxide grains in the size range 10 to 20 nm. Selected-area diffraction, Fig. 3, from the oxidized region reveals rings corresponding to NiO. Weak Cr_2O_3 and $NiCr_2O_4$ spinel reflections are also visible. The intensity of the ring pattern indicates that NiO is the predominant species. Cr_2O_3 grains are preferentially nucleated at the alloy grain and twin boundaries.

Increasing the temperature from 600 to 1000° C greatly increases the oxidation rate and also accelerates the formation of Cr_2O_3 and $NiCr_2O_4$ spinel oxides. As shown in Fig. 4a, the foil has been fully oxidized after heating the foil specimen to 1000° C in 10 torr O_2 and holding it there for 20 sec. The oxide grain size is approximately 100 to 500 nm. The diffraction pattern from this area, shown in Fig. 4b, reveals diffraction rings corresponding to Cr_2O_3, $NiCr_2O_4$ spinel and NiO. The spinel and NiO oxides are difficult to distinguish from each other because their diffraction rings overlap each other closely. Compared to the oxidation at 600° C there appears to be enhanced formation of Cr_2O_3 and interaction between Cr_2O_3 and NiO to form the spinel oxide.

3.2. Nucleation and early oxide growth on yttrium-implanted Ni–20% Cr

The yttrium-implanted specimens were subjected to *in situ* oxidation at 500° C in 10 torr O_2. Before oxidation, the alloy had been examined by AEM to check the distribution of yttrium. Energy dispersive spectrographic (EDS) analysis indicated the yttrium concentration to be around 4 wt % with uniform distribution in the thin section of the TEM foil. Ion implantation caused a great deal of lattice damage, as indicated by the strain contrast in Fig. 5. This damage is only observed in the surface layer, whereas the bulk alloy still has its original damage-free structure.

When the sample was heated to 550° C in 1 torr O_2,

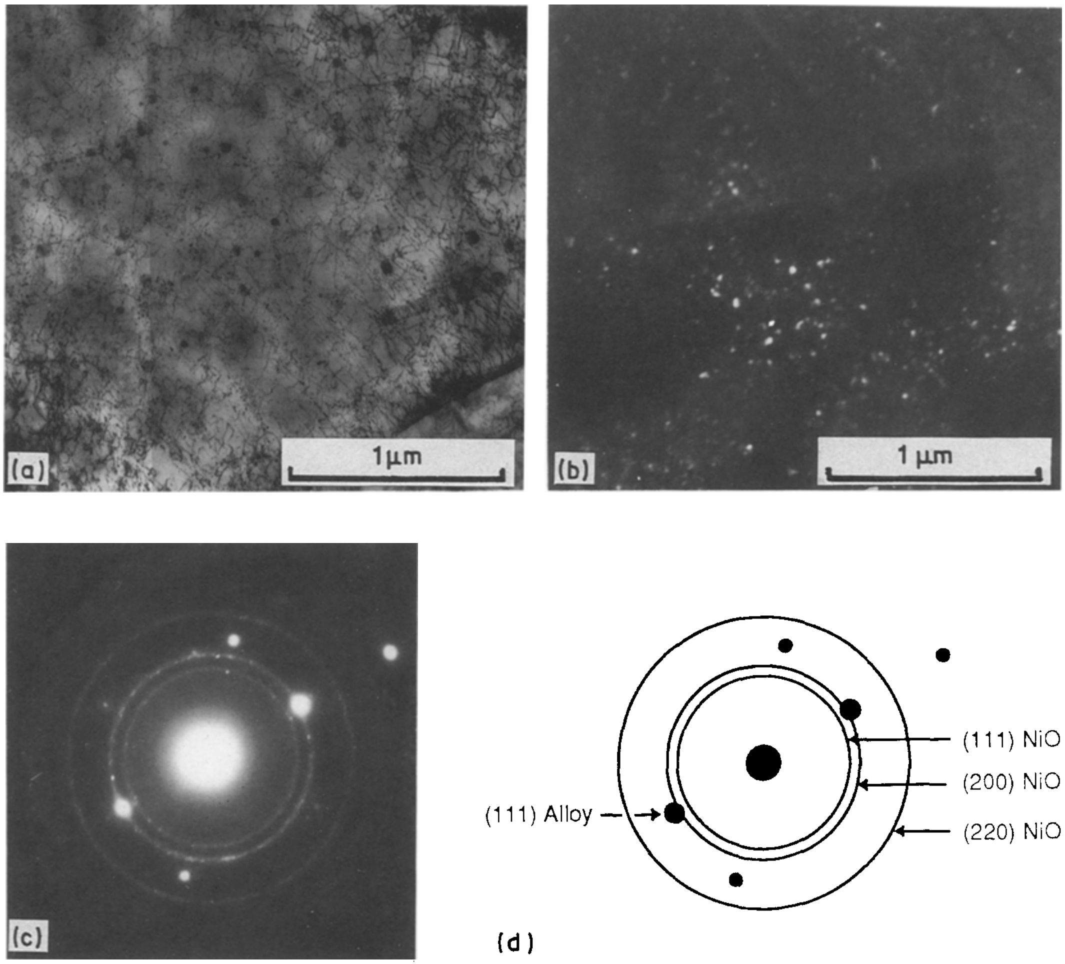

Figure 1 Ni–20% Cr oxidized *in situ* at 500 to 600° C in 10 torr O_2: (a) bright-field image showing NiO oxide nuclei within an alloy grain and at the grain boundary. (b) Dark-field image using $(1\,1\,1)_{NiO}$ diffracted beam. (c) Corresponding diffraction pattern and (d) indexed diagram obtained after 15 min oxidation. The spotty diffraction rings are from randomly oriented NiO crystallites.

the oxide nucleation rate and the initial growth were faster on yttrium-implanted samples than on unimplanted samples. For example, the thin section of an yttrium-implanted TEM foil was fully oxidized at 550° C after only 16 min exposure. We assume that the faster oxidation was due to the radiation damage which provides stored strain energy to accelerate the oxidation reaction. The fine-grained nature of the oxide scale is presented in Fig. 6. The average grain size is between 20 and 30 nm. Because of the rapid oxidation over the entire alloy surface, the location of the initial oxide nuclei could not be determined. The oxide is separated into regions of dark and light contrast. Possibly the light areas in the bright-field image correspond to regions where the TEM foil has been totally oxidized, as suggested by Flower and Wilcox [8].

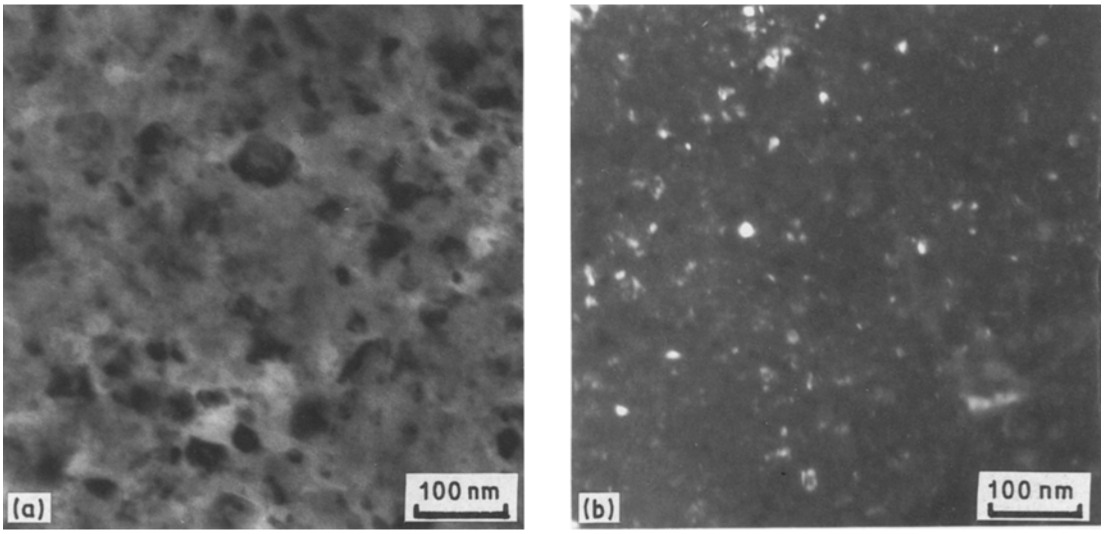

Figure 2 Ni–20% Cr foil oxidized *in situ* for 2 h at 600° C in 10 torr oxygen: (a) bright field image; (b) dark-field image, showing predominantly NiO of 10 to 30 nm grain size.

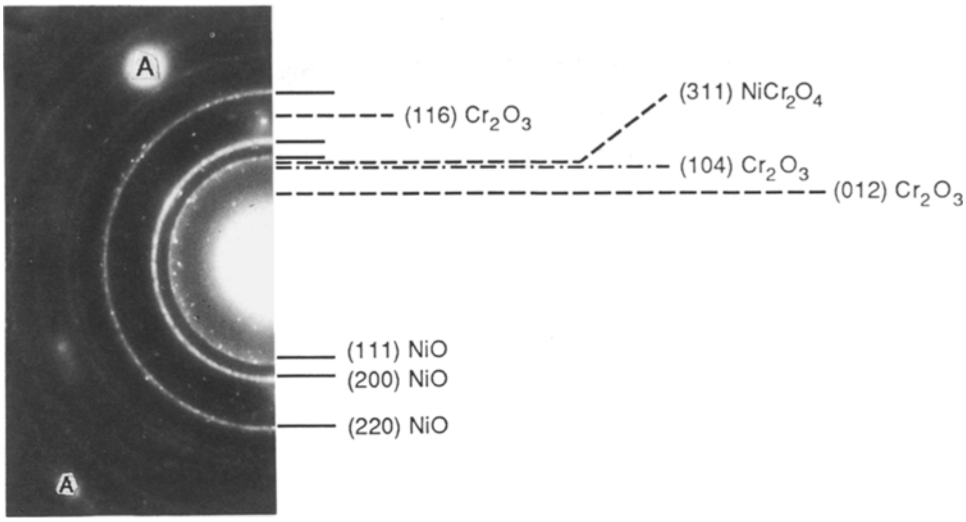

Figure 3 Selected-area diffraction pattern of an oxidized Ni–20% Cr TEM foil specimen corresponding to Fig. 2, showing diffraction rings from randomly oriented NiO with some $NiCr_2O_4$ and Cr_2O_3. The spots marked A are from the alloy.

The selected-area diffraction patterns in Fig. 7 are from an yttrium-implanted and oxidized alloy grain. Fig. 7b reveals that the early oxide includes NiO, $NiCr_2O_4$ spinel and Cr_2O_3. The strong diffraction spots of NiO indicate that it is the predominant oxide phase. The intensities of the Cr_2O_3 reflections increase at the foil edge and in the light areas of Fig. 6a. Two types of oxide orientations are found in different regions of the specimen. In the very thin areas of the TEM foil a ring pattern is obtained, Fig. 7b, indicating that the NiO and Cr_2O_3 are randomly oriented. On the other hand, the SADP taken from a thick area of the foil, which contains the implanted surface layer as well as large undamaged alloy grains, indicates highly oriented oxides. The epitaxial orientation relationship is revealed by comparing the electron diffraction patterns in Figs 7a and b, taken from the same region before and after oxidation. The strongest diffraction spots are from the [0 1 1] zone of NiO. It is parallel to the [0 1 1] zone from prior alloy grain. The epitaxial relationship is equivalent to that found by Hobbs *et al.* [11] for the NiO/Ni system. The indexed pattern shown in Fig. 7c indicates that $NiCr_2O_4$, having spots of lower intensity, is oriented parallel to the NiO, i.e., $[0\,1\,1]_{\mathrm{NiO}} \| [0\,1\,1]_{\mathrm{S}}$, where s = spinel. The reflections from the Cr_2O_3 are so weak that only four $\{0\,1\,.\,2\}$ spots are visible. The weakness of the other Cr_2O_3 diffraction spots makes it difficult to identify the zone axis. The *d*-spacings are such that the $(3\,0\,.\,0)$ diffraction spots of Cr_2O_3 could overlap with those of $(0\,\bar{4}\,4)_{\mathrm{S}}$ and $(0\,\bar{2}\,2)_{\mathrm{NiO}}$. The corresponding *d*-spacings for the above three planes are: 0.143 nm for $(3\,0\,.\,0)_{Cr_2O_3}$, 0.1471 nm for $(0\,\bar{4}\,4)_{\mathrm{S}}$ and 0.1476 nm for $(0\,\bar{2}\,2)_{\mathrm{NiO}}$. Similarly, the $(0\,0\,.\,6)_{Cr_2O_3}$, $(4\,0\,0)_{\mathrm{S}}$ and $(2\,0\,0)_{\mathrm{NiO}}$ diffraction spots could overlap. Even so, the angles between the four $\{0\,1\,.\,2\}$ spots of Cr_2O_3 are such that they cannot belong to the same zone. Therefore, at least two variants must be present. The likely orientation relationship between α-Cr_2O_3, $NiCr_2O_4$-spinel and NiO is then: $[0\,\bar{1}\,1]_{\mathrm{NiO}} \| [0\,\bar{1}\,1]_{\mathrm{S}} \| [1\,0\,.\,0]_{Cr_2O_3}$, which are also the closed-packed directions of fcc and hcp structures. Along with the distinct spots, a ring pattern

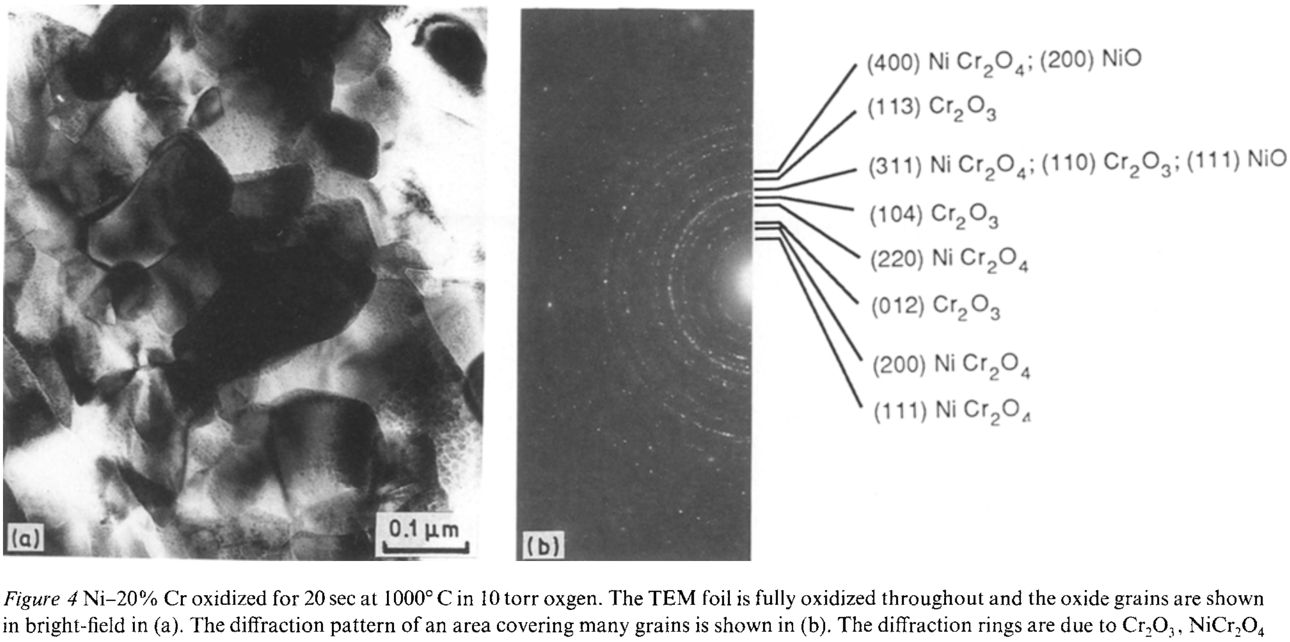

Figure 4 Ni–20% Cr oxidized for 20 sec at 1000° C in 10 torr oxgen. The TEM foil is fully oxidized throughout and the oxide grains are shown in bright-field in (a). The diffraction pattern of an area covering many grains is shown in (b). The diffraction rings are due to Cr_2O_3, $NiCr_2O_4$ and NiO. The latter two are difficult to distinguish.

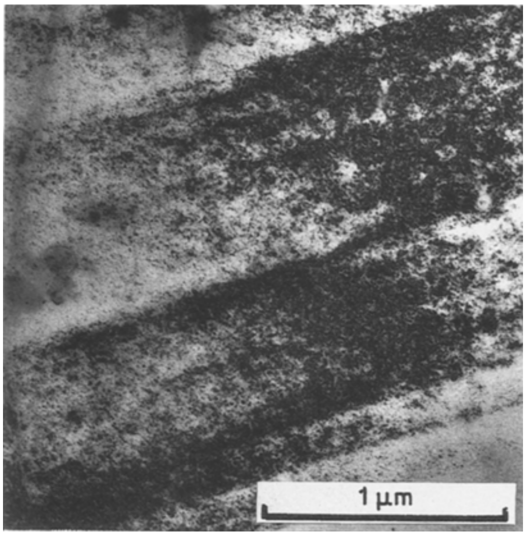

Figure 5 Yttrium ion-implanted alloy before oxidation: bright-field image showing fine contrast due to radiation damage.

of NiO is also seen in the SADP, indicating the presence of randomly oriented NiO crystallites. The oxide orientations from different areas of the foil and the overlap of oriented and random oxides will be discussed in more detail later. Summarizing, some oxide grains grow epitaxially on the yttrium-implanted alloy when the alloy substrate contains undamaged grains below the implantation zone, but on very thin foil cross-sections which contain only the ion-implanted layer, the oxide nucleates and grows with random orientations.

4. RBS results

Figure 8 shows a RBS spectrum from the yttrium-implanted Ni–20% Cr alloy before oxidation. The signals from the elements nickel and chromium are shown as steps with leading edges at 1.444 and 1.399 MeV, respectively. The yttrium signal has a Gaussian distribution with a peak at 1.482 MeV and a full-width half-maximum (FWHM) of 81.1 keV. The peak is below the leading edge (E_Y = 1.589 MeV) by 66.35keV. The data extracted from Fig. 8 are

H_{Ni} = 3093 counts, H_{Cr} = 535 counts, H_Y = 301 counts,

A_Y = 10022 counts, ΔE_Y = 66.35 keV, FWHM = 81.1 keV.

E_0 = 1.9 MeV, normal incidence with detection angle $\theta = 135°$ and channel width ε = 1.18 keV; where H is the height at the leading edge for each element, and A_Y is the number of counts under the yttrium peak. The various parameters are

$$[\varepsilon_0]_{Ni} = 71.5 \times 10^{-15}\,\mathrm{eV\,cm^2},\ K_{Ni} = 0.76,$$

$$[\varepsilon_0]_Y = 91.5 \times 10^{-15}\,\mathrm{eV\,cm^2},\ K_Y = 0.8364$$

$$(\mathrm{d}\sigma/\mathrm{d}\Omega)_Y = 7.851 \times 10^{-24}\,\mathrm{cm^2/sr},$$

$$(\mathrm{d}\sigma/\mathrm{d}\Omega)_{Ni} = 4.026\ \ 10^{-24}\,\mathrm{cm^2/sr}$$

where ε_0, K and $\mathrm{d}\sigma/\mathrm{d}\Omega$ are, respectively, the stopping cross-sections, kinematic factors for the mass ratio and Rutherford scattering cross-section. The composition of the bulk alloy can be determined by using the so-called surface energy approximation [10], where the ratio of nickel and chromium content is determined from the ratio of counts at their leading edges in the RBS spectrum. We also assume a uniform distribution of these elements. The density ratio $\varrho_{Ni}/\varrho_{Cr}$ can be obtained from the ratio of the heights of the leading edges using the following equation

$$\frac{\varrho_{Ni}}{\varrho_{Cr}} = \frac{H_{Ni}}{H_{Cr}} \frac{(\mathrm{d}\sigma/\mathrm{d}\Omega)_{Cr}}{(\mathrm{d}\sigma/\mathrm{d}\Omega)_{Ni}} \simeq \frac{H_{Ni}}{H_{Cr}} \left(\frac{Z_{Cr}}{Z_{Ni}}\right)^2$$

The value for $\varrho_{Ni}/\varrho_{Cr}$ indicates that the alloy contains approximately 20 wt % Cr, which is identical to the alloy composition.

Assuming the yttrium is in the top layer, the surface energy approximation can be used in calculating the stopping cross-section and the differential cross-section. The dose implanted at a rate of N in time t can be obtained from the equation:

$$\begin{aligned}(Nt)_Y &= (A_Y/H_{Ni,Cr})[\sigma_{Ni}(\mathrm{E}_0)/\sigma_Y(E_0)](\varepsilon/[\varepsilon_0]_{Ni}) \\ &= (A_Y/H_{Ni,Cr})(Z_{Ni}^2/Z_Y^2)(\varepsilon/[\varepsilon_0]_{Ni}) \\ &= 2.5 \times 10^{16}\,\mathrm{ion\,cm^{-2}}\end{aligned}$$

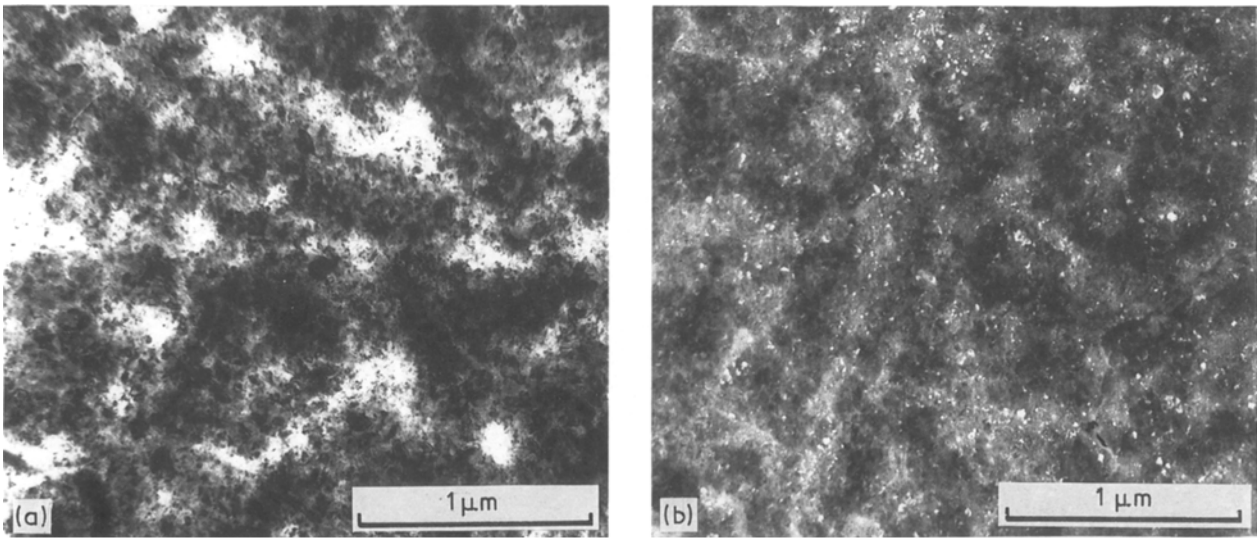

Figure 6 Yttrium-implanted Ni–20% Cr oxidized *in situ* at 500° C in 1.5 torr O_2 for 36 min: (a) bright-field and (b) dark-field image of oxide grains. The grain size is 10 to 50 nm.

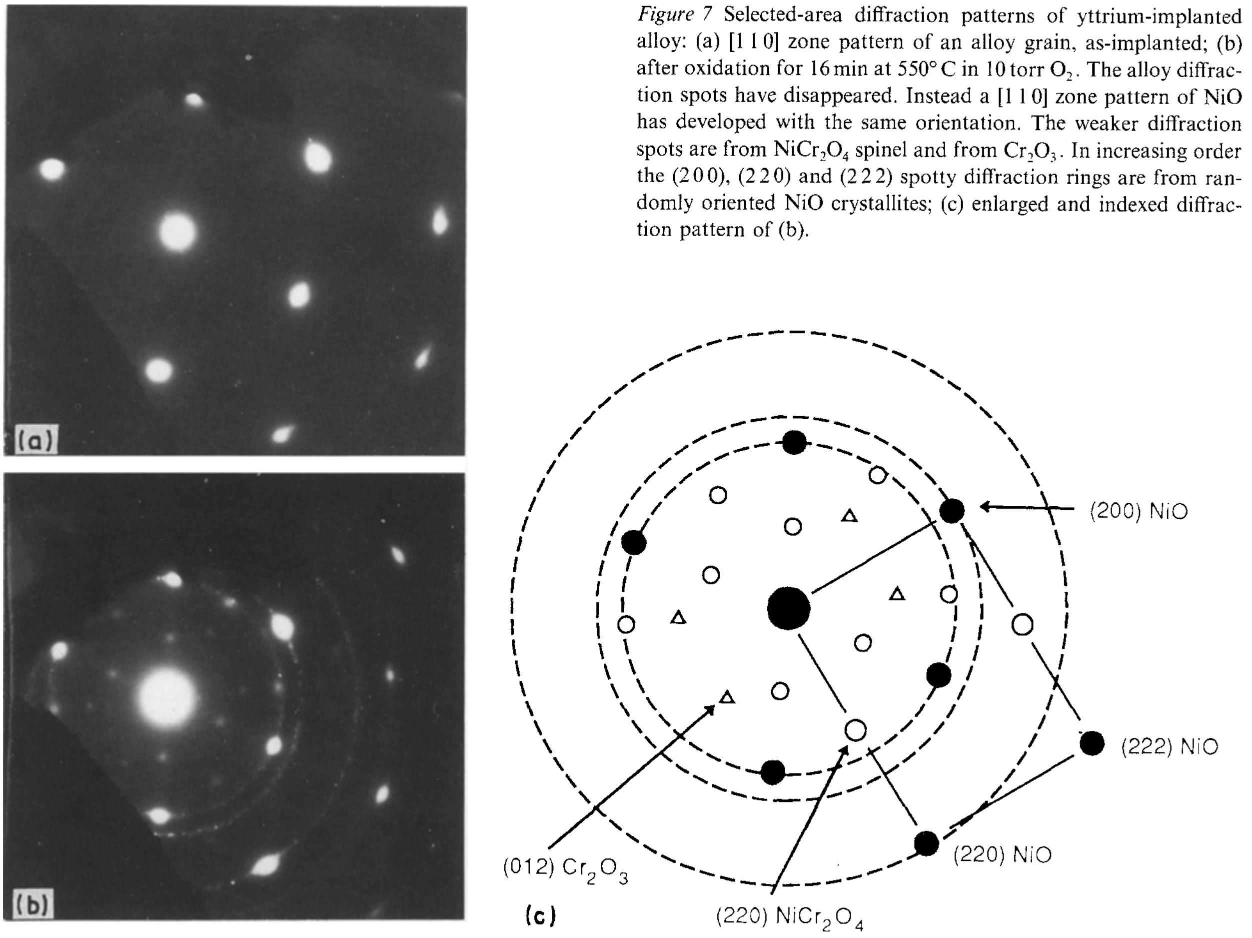

Figure 7 Selected-area diffraction patterns of yttrium-implanted alloy: (a) [1 1 0] zone pattern of an alloy grain, as-implanted; (b) after oxidation for 16 min at 550° C in 10 torr O_2. The alloy diffraction spots have disappeared. Instead a [1 1 0] zone pattern of NiO has developed with the same orientation. The weaker diffraction spots are from $NiCr_2O_4$ spinel and from Cr_2O_3. In increasing order the (2 0 0), (2 2 0) and (2 2 2) spotty diffraction rings are from randomly oriented NiO crystallites; (c) enlarged and indexed diffraction pattern of (b).

where we assume that the scattering cross-section, σ, and stopping cross-section, ε_0, of the alloy is represented by nickel. More accurately, the stopping cross-section for the alloy is given by $[\varepsilon_0]_{\text{Ni-Cr}} = 80/58.71\ [\varepsilon_0]_{\text{Ni}} + 20/51.996\ [\varepsilon_0]_{\text{Cr}}$ but this changes the results by less than 1%.

The concentration of yttrium in the alloy can be estimated from the peak height of the yttrium signal. Using the formula for bulk impurities and the above data, the fraction of yttrium atoms in the alloy is

$$\frac{N_Y}{N_{\text{Ni-Cr}}} = \frac{H_Y}{H_{\text{Ni-Cr}}} \frac{\sigma_{\text{Ni}}(E_0)}{\sigma_Y(E_0)} \frac{[\varepsilon_0]_Y}{[\varepsilon_0]_{\text{Ni-Cr}}}$$

Furthermore, the yttrium-concentration profile across the surface layer can be obtained from the shifting of the peak position $\Delta E_Y = 66.35$ keV using the formula

$$N_{\text{Ni-Cr}}\, R_P = E/[\varepsilon_0]_{\text{Ni-Cr}}$$

where R_P is the projected range of the implanted yttrium. In the present case, the distribution of implanted elements is Gaussian with range R_P and range straggling ΔR_P.

The computer program written for the above calculation by Averback [9] basically follows the same sequence. Firstly we can divide up the surface region as it comprises several distinct layers. The thickness of each layer is estimated from the RBS spectrum using the computer program where the channel number

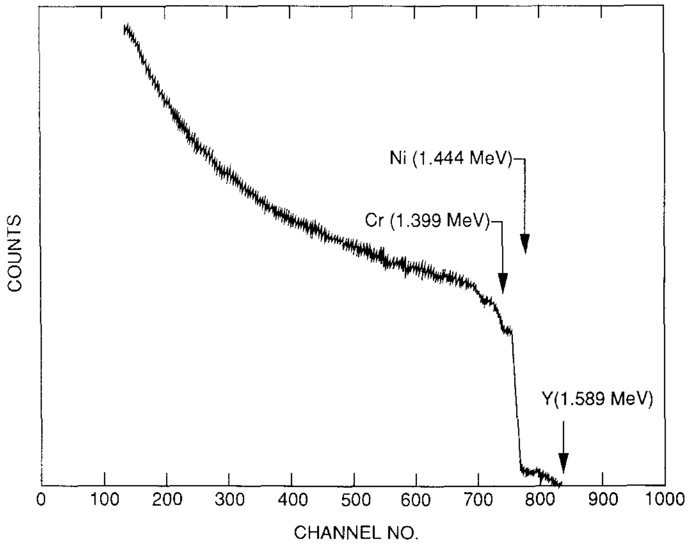

Figure 8 RBS spectrum of yttrium-implanted Ni–20% Cr alloy.

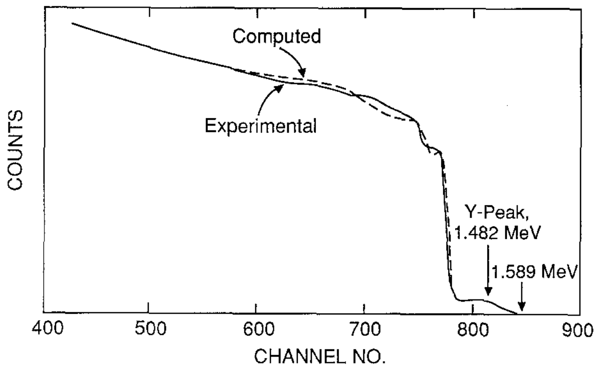

Figure 9 The high energy end of the experimental RBS spectrum of Fig. 8 (——) is compared with a computer-simulated RBS profile (- - -).

on the energy axis corresponds to a thickness of 0.14 nm per channel. Subsequently, the composition of yttrium, nickel and chromium is obtained from the ratio of counts in the same layer. A trial solution for the yttrium, nickel and chromium composition is then used to derive a RBS spectrum, which is then compared with the experimental RBS spectrum. If the simulated spectrum does not match the experimental spectrum, the input information has to be changed until the spectra do match.

The simulated spectrum is shown in Fig. 9 as a dashed line, and the comparison with the experimental spectrum is good. Based on this calculation, the total number of implanted ions is estimated to be 1.5×10^{16} ion cm^{-2}. The difference to the actual implant dose of 2×10^{16} ion cm^{-2} may be due to sputtering which has removed a few nanometres of material from the surface during the implantation procedure. The RBS data indicate that yttrium is concentrated in the 40 nm range beneath the surface with a maximum concentration of 3 wt %.

4.1. Oxide growth sequence on yttrium-implanted alloys, determined from RBS

The RBS spectra from an yttrium-implanted Ni–20% Cr specimen, oxidized for 1 and 5 min at 800° C under 20 torr O_2, are shown in Fig. 10. In Fig. 10a the experimental RBS spectrum of an oxidized specimen is compared with a computed spectrum to show the agreement. The experimental spectra of specimens, oxidized for 1 and 5 min, are plotted in Fig. 10b. Four important changes occur in the spectra of oxidized specimens relative to the spectrum of the unoxidized alloy.

1. The nickel counts at the leading edge are sharply reduced. This indicates that the nickel concentration has decreased from the bulk concentration of 80 wt %. Dilution with oxygen and an increase of chromium concentration due to preferential oxidation are the causes.

2. The height of the leading chromium edge is increased. The chromium peak shows that there is a chromium-rich surface oxide layer below which the chromium concentration drops to the bulk concentration of the alloy, as indicated by the decreasing chromium yield below the surface peak.

3. An oxygen signal occurs (not shown), with a leading edge typical for oxygen atoms at the surface of the specimen. The peak has a limited width from the thickness of the oxide film.

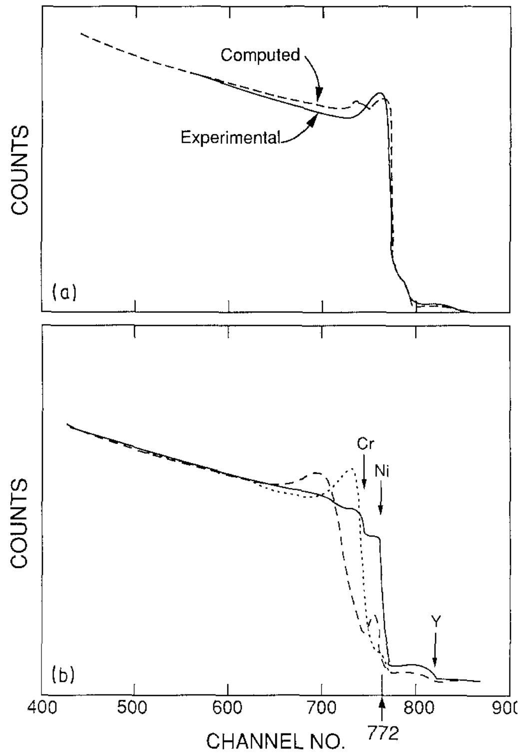

Figure 10 (a) The computed and experimental RBS spectra of yttrium-implanted Ni–20% Cr alloy, oxidized at 800° C, in 20 torr O_2 for 1 min. (b) Spectra taken from yttrium-implanted Ni–20% Cr alloy after oxidations from (——) 0, (····) 1, and (– – –) 5 min at 800° C in 20 torr oxygen.

4. The yttrium peak shifts inward and spreads. The yttrium-concentration profile is shown in Fig. 11 after oxidation in comparison with the original implanted distribution. Most of the yttrium is concentrated in the oxide scale. Because several different oxides (NiO, $NiCr_2O_4$, Cr_2O_3, Y_2O_3 and perhaps other compounds) may form, it is impossible to determine the ratio of each element to oxygen just by comparing the surface height of the oxygen and chromium peaks, for example.

After increased oxidation time for 5 min under the same conditions, the yttrium is still at its original position, as shown in Fig. 10. The modest increase of the nickel edge indicates that there is more NiO accumulated at the surface. The leading edge of chromium has shifted to a lower energy, which indicates that chromium is no longer present at the specimen surface. The Cr_2O_3 oxide is underneath the NiO layer.

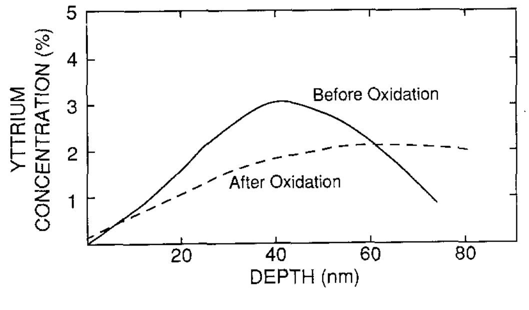

Figure 11 The yttrium distribution determined from RBS spectra before and after oxidation at 800° C, 20 torr O_2 for 1 min.

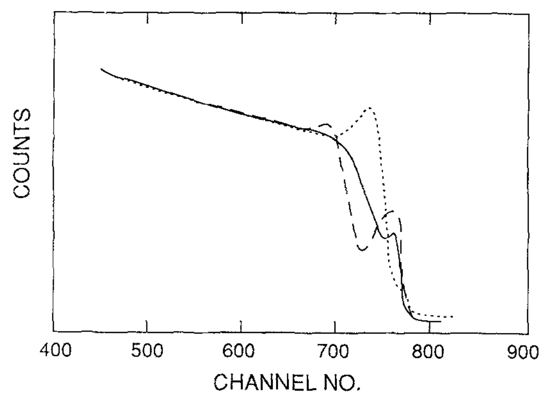

Figure 12 RBS spectra from unimplanted alloy oxidized at 800° C in 20 torr O_2 for (——) 1 min and (- - -) 5 min. (· · · ·) The spectrum of a 1 min oxidized yttrium-implanted specimen shown for comparison.

The shift is very pronounced in the RBS spectra of Fig. 10b. The distribution of the alloy elements before and after oxidation for periods of 1 and 5 min is also obtained from Fig. 10, and in Fig. 11 the yttrium-distributions are shown. Based on this information the formation of the oxide scale is thought to occur in the following sequence: the first oxide formed on the surface contains a chromium concentration which is higher than that of the bulk alloy. Subsequently, nickel diffuses through the initially formed Cr_2O_3-rich scale to form an NiO scale at the oxide/gas interface.

4.2. Oxide growth sequence on unimplanted alloy, determined from RBS

Under identical oxidation conditions, 800° C and 20 torr O_2, the sequence of scale development is opposite on an unimplanted alloy to that on an yttrium-implanted alloy. Two RBS spectra from oxidized unimplanted samples are shown in Fig. 12 and compared with the spectrum of an yttrium-implanted specimen after oxidation for 1 min. The first oxide (1 min oxidation) on the unimplanted alloy is mostly NiO. The decrease in the height of the leading nickel edge is due to dilution with oxygen. The shift of the leading chromium edge to a lower energy indicates absence of chromium at the surface. Beneath the NiO there is no increase of chromium concentration, and the Cr_2O_3 oxide content is assumed to correspond to the chromium concentration of the alloy. After oxidation for 5 min, the nickel peak has increased, which means the amount of NiO in the scale has increased. A slight chromium peak is observed at a relatively low energy (~ channel 700), representing a concentration of Cr_2o_3 below the NiO scale. Apparently, the concentration of Cr_2O_3 has increased in a layer between the NiO scale and the alloy substrate.

4.3. Summary of RBS information

The results of semi-quantitative analyses of the RBS data by computer simulation of the spectra are summerized in Table I.

For the Ni–Cr sample, the oxide scale formed after 1 min exposure is almost all NiO with a thickness of approximately 75 nm. After 5 min exposure the scale develops into two layers. The outer layer (the surface oxide) is NiO with a thickness of ~ 70 nm, and the inner layer begins to be enriched with Cr_2O_3. By comparison, the first oxide formed on the yttrium-implanted alloys (1 min exposure) is ~ 69% Cr_2O_3 with a thickness of 42.5 nm. The yttrium, presumably in the form of Y_2O_3 is concentrated inside this oxide. Extending the exposure to 5 min, the oxide scale develops also into two layers. However, the outer layer with a thickness of only 17.5 nm maintains a significant (50%) Cr_2O_3 content while the inner layer adjacent to the alloy substrate incorporates Y_2O_3 and develops a rather high Cr_2O_3 concentration (75%). It appears that implanted yttrium enhances the nucleation of Cr_2O_3 during the first oxidation exposure. During continued oxidation a high concentration of Cr_2O_3 is maintained at the scale/alloy interface.

The data from the above calculation are semiquantitative. They could change depending on several parameters, such as the assumed density. For the calculation, the density of oxide has been assumed to equal that of the Ni–20% Cr alloy. It actually should be modified when the oxide forms on the surface. Also, because there is overlap of the yttrium and nickel peaks, especially after inward diffusion of yttrium during oxidation, it is difficult to find an exact location for the small amount of yttrium. Therefore, the data in Table I provide only a rough estimation of the distribution of nickel, chromium and yttrium after different exposure times. Also, the RBS technique cannot provide any information about the oxide structures, e.g. whether the oxides are NiO, Cr_2O_3 or $NiCr_2O_4$. For simplicity, therefore, the results in Table I are given as percentages of NiO and Cr_2O_3 only.

TABLE I Semiquantitative results of oxide compositions from RBS data. Oxide scales were formed in 1 and 5 min oxidation treatments at 800° C in 20 torr O_2 atmosphere

Oxidation time (min)	Unimplanted alloy	Y-implanted alloy
0 min	Alloy: 80%Ni, 20%Cr	Alloy: 77%Ni, 19%Cr, 4%Y
1 min	Single oxide layer, 74.5 nm thick consisting of 90%NiO, 10%Cr_2O_3	Single oxide layer, 42.5 nm thick consisting of 26%NiO, 69%Cr_2O_3, 5%Y_2O_3
5 min	Double layer, 120 nm thick Outer 70 nm thick layer consists of 95%NiO, 5%Cr_2O_3 Inner 50 nm thick layer consists of 61%NiO, 39%Cr_2O_3	Double layer, 67.5 nm thick Outer 17.5 nm thick layer consists of 49%Cr_2O_3, 2%Y_2O_3, balance NiO Inner 50 nm thick layer consists of 20%NiO, 75%Cr_2O_3, 5%Y_2O_3

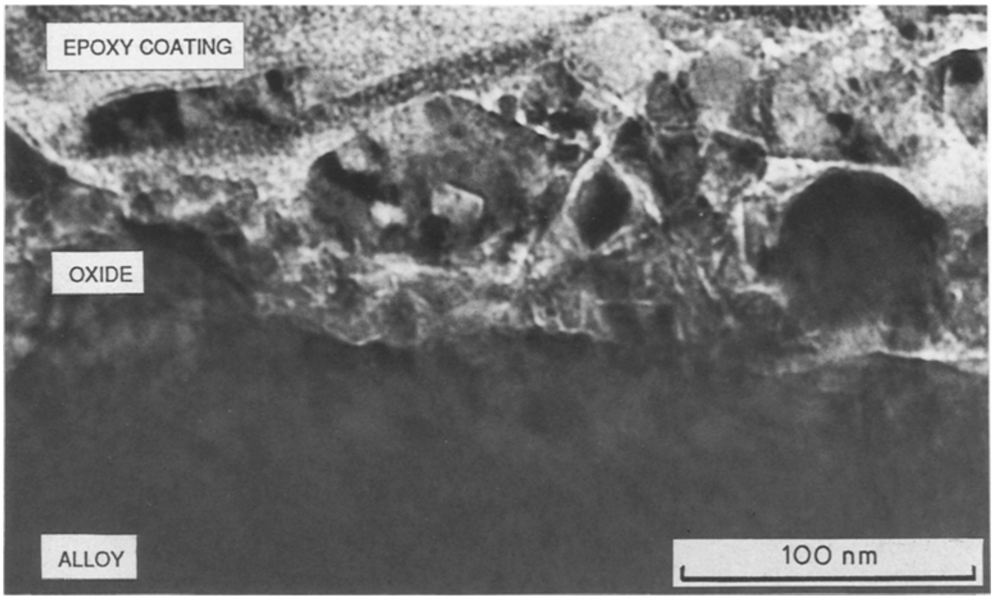

Figure 13 Bright-field TEM image of a transverse cross-section through the oxide scale on yttrium-implanted alloy, oxidized for 1 min at 800° C in 20 torr oxygen, showing a single fine-grained (10 to 50 nm) oxide layer.

5. Analytical electron microscopy on transverse cross-sections

The compositions of the initial oxide films on yttrium-implanted and unimplanted Ni–Cr have been determined by the RBS results. However, the existence of several distinct layers, each with a unique microstructure and morphology is not detected by the RBS technique. The layers are best analysed by transmission electron microscopy on transverse section thin films. This not only reveals the scale microstructure but also yields microchemical data which can be compared with the semi-quantitative data from the RBS investigation.

5.1. Oxide film formed at 800° C on yttrium-implanted alloy

A uniform and adherent oxide film with a thickness from 50 to 100 nm forms on the yttrium-implanted alloy after 1 min oxidation at 800° C. In the transverse cross-section (Fig. 13), the oxide film appears as very fine grained or featureless. The grain size is between 10 and 50 nm. Selected-area diffraction showed that the oxide contains NiO and Cr_2O_3, and occasional extra reflections correspond to Y_2O_3. The alloy/oxide interface is slightly corrugated.

Energy-dispersive spectroscopy (EDS) of X-rays from the oxide film indicates that its chromium content is higher than the nickel content, Fig. 14. An yttrium peak is also visible. With the assumption that the elements are all in the form of oxides, the analysis of the spectrum indicates that the oxide is composed of 51 wt% Cr_2O_3, 40 wt% NiO and 9 wt% Y_2O_3. These values are slightly different from the RBS data, but are considered to be consistent with them. EDS analysis on the alloy substrate adjacent to the oxide film shows that the alloy maintains its original composition, with a very small amount of yttrium present. Apparently most of the yttrium has been incorporated into the oxide film. It is of interest to know whether Y_2O_3 is concentrated at grain boundaries or within NiO or Cr_2O_3 oxide grains. However, its precise location could not be detected due to limitation of the spatial resolution of the EDS. The smallest EDS probe size in TEM was about 40 nm.

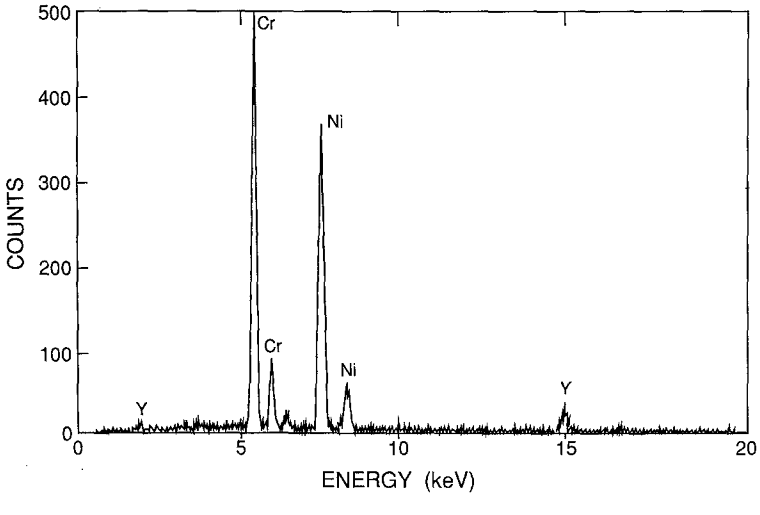

Figure 14 Energy-dispersive X-ray spectrum from the oxide of yttrium-implanted alloy oxidized for 1 min at 800° C in 20 torr oxygen. The oxide contains more chromium than nickel and also some yttrium.

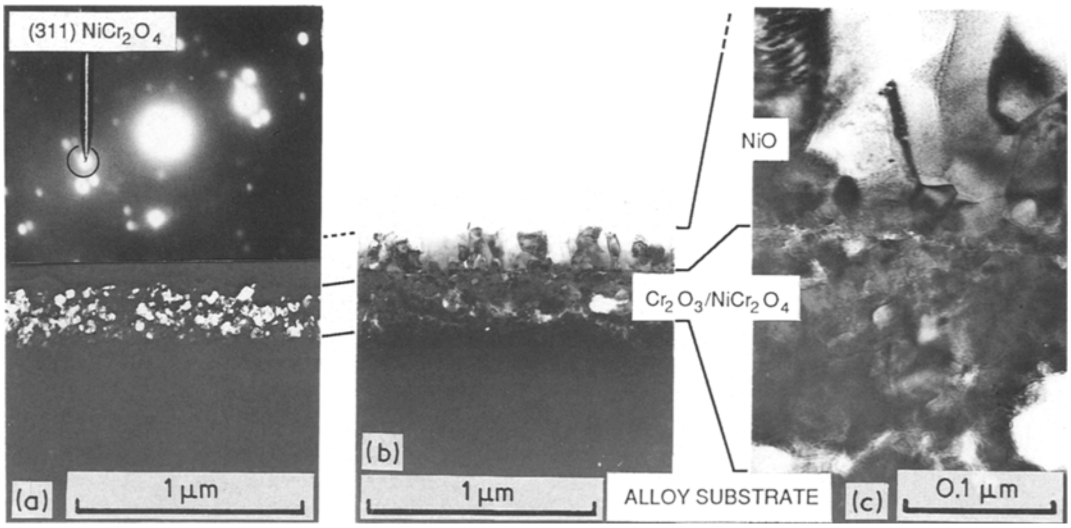

Figure 15 Transverse section through oxide scale on Ni–20% Cr after 1 min oxidation at 1000° C in 1 atm O_2. The scale consists of two oxide layers, an inner $Cr_2O_3/NiCr_2O_4$ layer and an outer NiO oxide layer. (a) Dark-field TEM image of the inner chromium-rich oxide layer taken with a (3 1 1) spinel deffracted beam showing the fine grain size (10 to 50 nm) in this layer. (b), (c) Bright-field images of the oxide scale showing the sharp microstructural transition between the two oxide layers. The $Cr_2O_3/NiCr_2O_4$ layer has fine, equiaxed grains, and there is some porosity at the oxide/alloy interface. The outer NiO oxide layer has a graduated microstructure, beginning with small (~ 50 nm) equiaxed grains and continuing outwards with columnar grains of ~ 100 nm width. Note, only a portion of the NiO layer is visible. Its outermost portion has been lost during sputter-thinning of the TEM foil.

5.2. Oxide films formed at 1000° C on yttrium-implanted and on unimplanted alloys

Double-layer oxide scales develop on both yttrium-implanted and unimplanted alloys. Their scale cross-sections after 1 min oxidation are shown in Figs 15 and 16. A double-layer scale composed of outer NiO and inner $Cr_2O_3/NiCr_2O_4$ is formed on the unimplanted alloy. The layers are separated by a distinct boundary. The NiO layer is columnar with a grain width of 50 to 100 nm. We are uncertain about the total thickness of the NiO layer because of sputter loss during specimen preparation. The inner spinel oxide layer is approximately 200 nm thick with fine grains (10 to 50 nm size) and some voids of similar size. The voids at the alloy/oxide interface weaken the adhesive strength. The selected-area diffraction pattern (SADP) in Fig. 15a shows diffraction spots of $NiCr_2O_4$ spinel and a few spots of Cr_2O_3 and NiO. The (3 1 1) spinel diffraction spot was used to generate the dark-field image of the inner oxide layer. Its thickness is ~ 250 nm.

The yttrium-implanted alloy also develops a double-layer oxide scale, Fig. 16. The outer layer consists of columnar grains of ~ 50 to 100 nm width and ~ 250 nm thickness. The oxide is NiO, as determined by EDS (over 90% Ni) and SADP analysis. The structure of the inner layer is like the one on the unimplanted alloy, but the layer is thicker (600 nm) and has no porosity. An SADP from this layer (not shown) indicates that the major oxide is Cr_2O_3 with some NiO and $NiCr_2O_4$ spinel. There is no sharply defined interface between alloy substrate and oxide, and the alloy may contain some (internally oxidized) Cr_2O_3 grains. The alloy substrate apparently is strained as indicated by the strain contrast and by dislocations near the interface. These observations indicate strong adherence between alloy and oxide. EDS results showed that the inner oxide layer contains 40 wt % Cr. Yttrium could not be detected at the alloy/oxide interface. However, when the probe was set at the interface between the inner and outer oxide layer, an yttrium peak was observed in EDS spectrum. From several such tests at different positions we conclude that the yttrium is concentrated near the interface region between the inner and outer oxide layers.

6. Discussion

The results of *in situ* oxidation experiments on thin foils in the TEM, of TEM observations through cross-sections of oxide scales on bulk samples, and of RBS on oxide films on bulk samples are summarized in Fig. 17. One influence of yttrium is the enhancement of initial oxide growth rate at low temperature (500° C). Possibly, the implantation-induced lattice defects in the alloy surface layer enhance cation mobility for fast initial oxide growth. At higher temperatures (800, 1000° C), however, there is no enhancement of oxide growth by the implantation. On the contrary, the RBS results show reduced oxide growth at 800° C for 1 min on the yttrium-implanted alloy. The TEM results of the oxides grown at 1000° C for 1 min show the inner Cr_2O_3-rich layer on yttrium-implanted alloy to be of the same thickness as on the unimplanted alloy. However, the growth of the outer NiO layer is slowed on the yttrium-implanted alloy. In the yttrium-implanted alloy, nucleation of Cr_2O_3 is favoured at every temperature. Nucleation of chromium-rich oxide, most likely spinel, is also enhanced in the unimplanted alloy at the higher oxidation temperature of 1000° C.

Some of the initial oxide on the yttrium-implanted specimen had an epitaxial relationship with the alloy substrate, but on very thin sections of the implanted TEM foils there was no orientation relationship. The development of an epitaxial relationship is thought to occur by preferential nucleation of certain orientations for which there is a low interfacial free energy. In

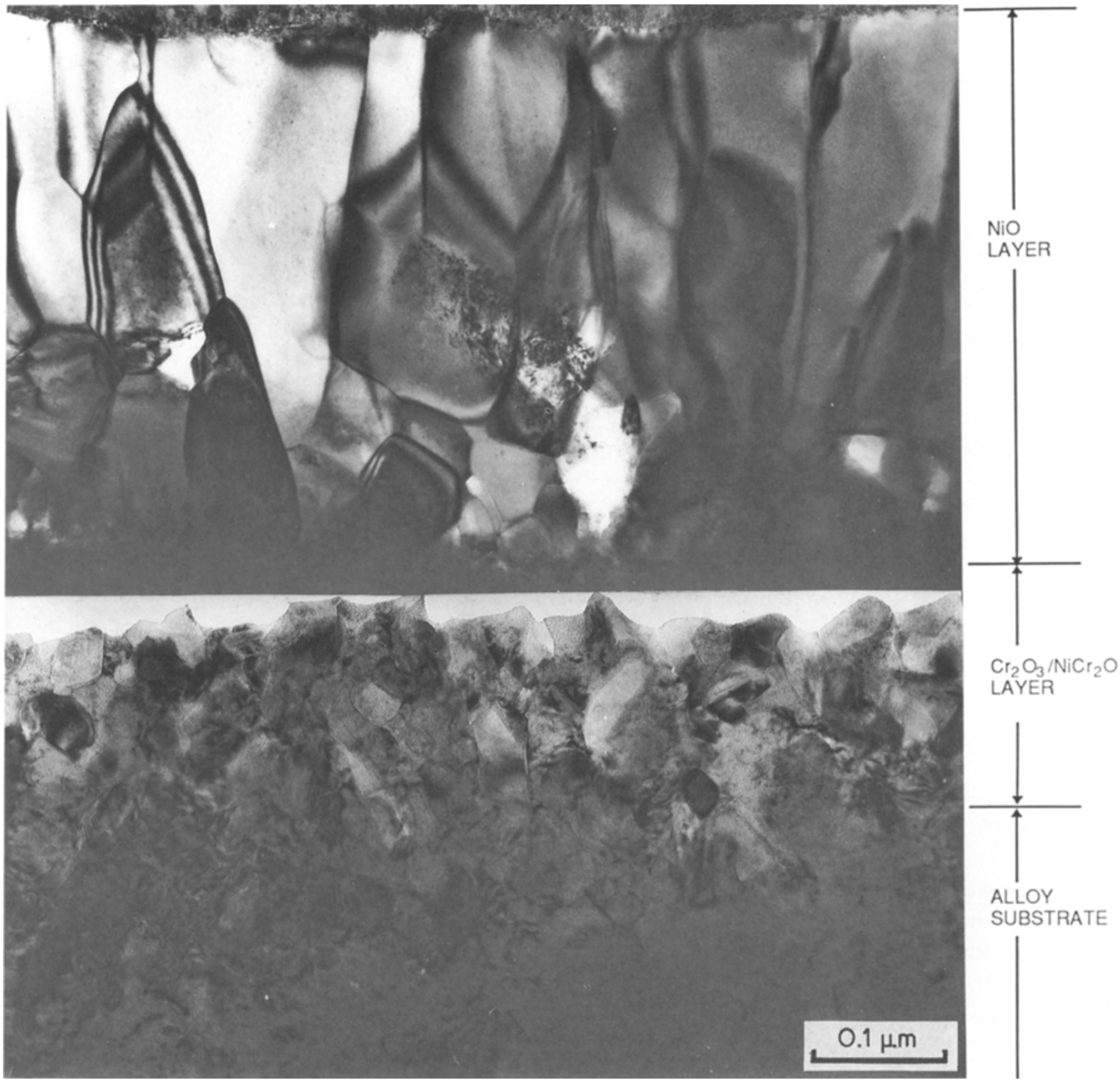

Figure 16 Montage of two TEM bright-field images showing the cross-section of the double layer oxide scale on yttrium-implanted Ni–20% Cr, formed after 1 min at 1000° C in dry air: the inner $Cr_2O_3/NiCr_2O_4$ layer has fine (10 to 50 nm) equiaxed grains and is fully dense. It has good adherence to the alloy substrate. The outer NiO oxide layer has a graduated microstructure, beginning with small (~ 50 nm) equiaxed grains and continuing outwards with columnar grains of ~ 100 nm width.

addition to Y_2O_3, three oxides can form on yttrium-implanted alloys in the initial stage of oxidation: α-Cr_2O_3, $NiCr_2O_4$ and NiO, each with varying amounts of nickel and chromium. The face-centred cubic NiO oxide grows in such a way that the cube orientations of oxide and metal are parallel. This is the same as on pure nickel [11]. The orientation relationship between the $NiCr_2O_4$ spinel and NiO is the same as that of the NiO to the alloy substrate. The lattice parameter of spinel is approximately twice that of the NiO (0.165% mismatch). The relationship between the cubic spinel (S) and the rhombohedral (R) Cr_2O_3 lattices is more complex. The results suggest that the $[30.0]_R$ direction is parallel to the $[0\bar{4}4]_S$ direction. According to Howes [12] and Cox *et al.* [13], the close-packed directions and the closed-packed planes of the anions are parallel in the two structures. The diffraction data in this work are consistent with this notion but are insufficient to prove it unequivocally. The better oxide adherence on yttrium-implanted alloy may, in part, be a consequence of the orientation relation.

In the implanted condition the yttrium concentration profile in the surface layer of the alloy is approximately Gaussian with a projected range, R_P, and a range straggling, ΔR_P. The computer evaluation of the RBS spectrum of yttrium-implanted Ni–20% Cr alloy gave values for R_P and ΔR_P of 40 and 50 nm, respectively. In comparison, calculated values of range and straggling of 280 keV Y^+ ions into nickel are 55 and 20 nm [14].

It is likely that the implanted yttrium is oxidized first because of its large negative free energy of oxide formation. The Y_2O_3 oxide has been speculated to also enhance nucleation and growth of Cr_2O_3 [15]. In our work a correlation between Y_2O_3 nuclei and Cr_2O_3 grains was not obtained, possibly because the very fine dispersion of Y_2O_3 was below the resolution limit of the EDS examination. Cr_2O_3 can form by solid state reaction between chromium from the alloy with NiO or spinel oxide. Y_2O_3 has a very low solubility in Cr_2O_3, and this has been used as an argument that it should segregate to the oxide grain boundaries and to the metal/oxide interface [16]. By "stuffing" Cr_2O_3 or spinel grain boundaries or other fast diffusion paths, the outward diffusion of chromium cations would be reduced such that it would no longer dominate the

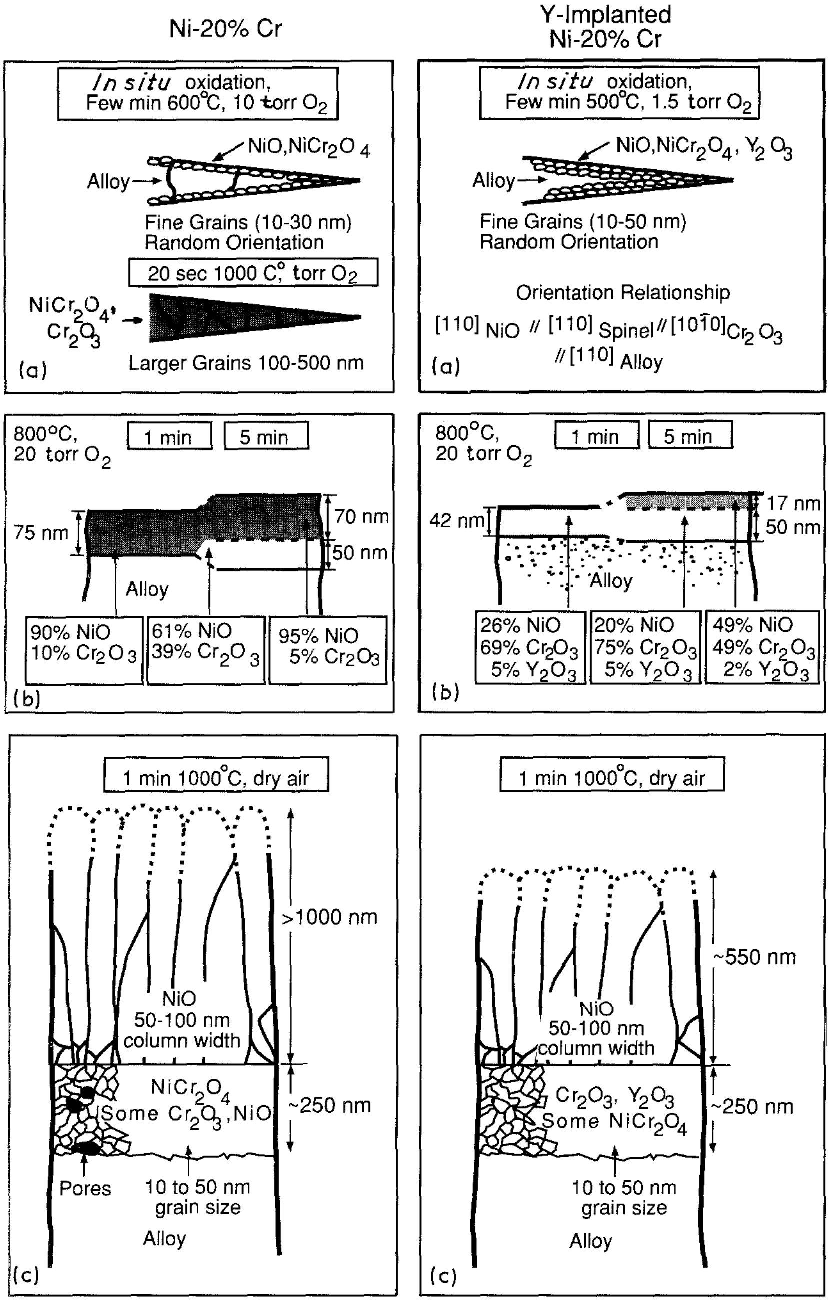

Figure 17 Summary of the oxidation results for unimplanted and for yttrium-implanted Ni–20% Cr: (a) *In situ* oxidation in TEM at 500 to 1000° C in 1 to 10 torr O_2. (b) RBS results of bulk samples oxidized at 800° C in 20 torr O_2. (c) TEM results from scale cross-sections on bulk samples, oxidized in air at 1000° C.

scale growth. In recent high-resolution AEM work by Bennett *et al.* [17] segregated Y_2O_3 has been detected in triple point junctions of spinel grains and along spinel boundaries.

Sequences of oxide growth can therefore be summarized as follows (see Fig. 18). An air-formed Cr_2O_3 film may exist on the unimplanted alloy before oxidation [18]. At elevated temperature fast diffusion of Ni^{2+} cations leads to the formation of an outer NiO layer with an initial fine-grained equiaxed structure progressing into an oriented columnar structure. With increasing thickness of the NiO layer the oxidation rate (assumed to be controlled by Ni^{2+} diffusion) slows down, and chromium is increasingly oxidized by reaction with the NiO and by reaction with inward diffusing O^{2-}. $NiCr_2O_4$ spinel or Cr_2O_3 are the phases of the inner oxide layer adjacent to the alloy substrate.

On the yttrium-implanted alloy the growth sequence is different. Initially, there may also be a thin air-formed Cr_2O_3 film. During high-temperature oxidation the yttrium presumably oxidizes first, i.e. there is Y_2O_3 in the alloy. Radiation damage and the presence of Y_2O_3 may enhance the rate of chromium oxidation over that of nickel oxidation. The result is a fine-grained Cr_2O_3–Y_2O_3 oxide layer with good adherence to the alloy. During scale growth, the Y_2O_3 oxide remains concentrated in the inner Cr_2O_3-rich layer and thus exerts its effect even after long-term oxidation, e.g. when the scale thickness is many times the original implant depth [7]. The oxidation rate of the implanted alloy is faster only at the beginning of oxidation at relatively low temperature, but for all other conditions the oxidation rate is reduced in the implanted alloy.

Y_2O_3 retards the outward diffusion of Cr^{3+} cations, thereby enabling the early formation of a dense inner Cr_2O_3 layer. This in turn slows the outward diffusion of Ni^{2+} and reduces the overall oxide growth rate. In the double-layer scales, the inner chromium-rich layer is generally much finer grained than the outer NiO layer. With the small grain size, grain boundaries are expected to play the dominant role in the mass transport across the scale. Fleetwood [19] suggested that even sub-grain boundaries are rapid diffusion paths

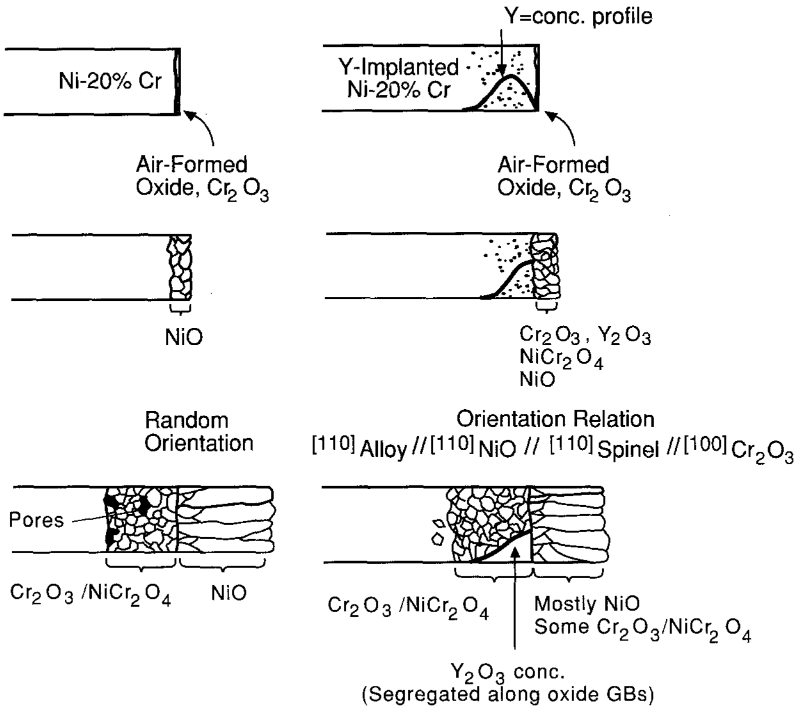

Figure 18 Oxide growth sequences on the unimplanted and yttrium-implanted alloy.

for chromium in the alloy, and, depending on the grain size, chromium diffusivity can vary by an order of magnitude [20, 21].

The experiments show the inner chromium-rich oxide layer is fine-grained on both unimplanted and yttrium-implanted specimens, but that the Cr_2O_3 content and the density are higher on the yttrium-implanted alloy. A model of the oxidation mechanism of the yttrium-implanted alloy must therefore include a diffusion barrier in the oxide grains and in the grain boundaries. The literature contains arguments for each. Laurent and Benard [22] suggested that grain boundaries in ionic solids are short-circuit paths for anions, but not for cations. Stringer *et al.* [2] suggested that dislocations are the short-circuit paths for the transport of Cr^{3+} through Cr_2O_3. Measurement of chromium self-diffusion has been conducted in single crystals of Cr_2O_3 by Hoshino and Peterson [23]. The results as a function of oxygen partial pressure indicate that Cr^{3+} cation diffusion occurs by a vacancy mechanism. Also the bulk diffusion coefficients deduced from measurements in Cr_2O_3 single crystals are a factor of 10^3 smaller than grain-boundary diffusion coefficients from polycrystalline Cr_2O_3. From these data it is obvious that grain-boundary diffusion dominates over bulk diffusion. The average Cr_2O_3 grain size on yttrium-implanted alloy is about 20 nm. If we put the grain boundary width as 1 nm, the grain-boundary diffusion flux should be about two orders of magnitude larger than the flux through the grains. The dislocation flux must be very small compared to the grain-boundary flux unless there is a large density of dislocations in the Cr_2O_3 grains, which has not been observed by TEM. The retardation of the oxide growth rate by Y_2O_3 can be explained by Y_2O_3 segregation to the oxide grain boundaries [17, 24] where it blocks fast diffusion [25].

A change in the direction of scale growth caused by alteration in the defect structure of Cr_2O_3 by Y_2O_3 additions has also been proposed. Cr_2O_3 is known to be a p-type semiconductor. The chromium-cation vacancies are the dominant mobile species in the oxidation of chromium. Michels [27] proposed that Y_2O_3, La_2O_3, ThO_2 and Al_2O_3 added to the alloy occupy cation vacancies in the Cr_2O_3 scale. This would reduce the total number of vacancy-type defects in Cr_2O_3 and lower the diffusion rate of the Cr^{3+} cations, and as a result improve the oxidation resistance. However, Nagai *et al.* [28] showed that the electrical conductivity of Cr_2O_3 increased when doped with La_2O_3 and Y_2O_3. Golightly *et al.* [29] suggested that yttrium occupies the aluminium lattice site in α-Al_2O_3 as a trivalent dopant with zero effective charge. Because Cr_2O_3 has the same crystal structure as Al_2O_3, theoretical calculations on the effects of Y^{3+} on diffusion in Al_2O_3 may be applicable here. For example, Anderson *et al.* [30] have used molecular orbital theory of atom clusters to show that yttrium atoms have a very strong binding energy to aluminium atoms, because of charge transfer from their high-lying valence orbitals to the low-lying nickel s–d band. This calculation also applies to nickel alloys containing aluminium with yttrium additions, and possibly the same mechanism can occur in Ni–Cr alloys and can explain the suppression of the outward cation diffusion in that chromium atoms are tied up by yttrium atoms.

7. Conclusions

7.1. Oxide nucleation and growth on Ni–20% Cr alloy

In the temperature regime 600 to 1000° C, NiO nucleates initially and forms very fine randomly oriented grains of 10 to 30 nm size. The nucleation is not significantly enhanced at sites where alloy grain boundaries intersect the surface. During further oxide growth, $NiCr_2O_4$ spinel and Cr_2O_3 develop a second layer below the NiO. At the higher temperature of 1000° C, some spinel and Cr_2O_3 form immediately along with NiO, and after prolonged oxidation time double-layered oxide scales form. The outer layer consists of columnar NiO grains (50 to 100 nm width), and fine (10 to 50 nm) equiaxed grains of chromium-rich oxide make up the inner layer. In the absence of a dopant the inner layer permits outward cation diffusion of Ni^{2+} and some Cr^{3+}. Much of this diffusion is believed to occur along oxide grain boundaries.

7.2. Oxide nucleation and growth on yttrium-implanted Ni–20% Cr

Implanted yttrium affects both the nucleation and the long-term growth of oxide. The effects are summarized below.

1. Nucleation of chromium-containing oxide is enhanced. This leads to an early protective oxide layer which slows outward cation diffusion and thus the entire oxidation process. With time a double-layer scale develops similar to that on unimplanted alloy. But there are important differences. The inner layer contains Y_2O_3 and has a higher chromium content. Its microstructure is equally fine-grained (10 to 50 nm grain size) as on unimplanted alloy, but is fully dense and it appears to have stronger adherence to the alloy substrate. With continued oxide growth the Y_2O_3 is distributed over the inner oxide layer. Although the Y_2O_3 concentration peak is thereby lowered and broadened, the yttrium remains concentrated in the inner layer near the interface with the outer NiO oxide layer. There it exerts its influence on cation diffusivity even after the scale has grown to a greater thickness than the original implantation depth.

2. Nucleation and initial growth of oxide is accelerated on the implanted alloy, but only at relatively low temperature (500 to 600° C). In all other cases the yttrium-implanted samples experience reduced overall oxide growth. The effect of yttrium is to slow outward cation diffusion through the inner oxide layer and to enhance the preferential oxidation of chromium. Arguments have been presented to account for reduced bulk and grain-boundary diffusivities. In view of the fine grain size of the inner oxide, a blocking mechanism of grain-boundary diffusion is necessary to explain the reduction of oxide growth by implanted yttrium. The microchemical analysis in STEM did not have sufficient spatial resolution to detect enrichment of Y_2O_3 at Cr_2O_3 or $NiCr_2O_4$ grain boundaries. However, other work suggests that such segregation occurs and is the cause of reduced cation diffusion.

3. Nucleation of the early oxide on Y-implanted alloy occurs in some instances (at 500° C in 1.5 torr oxygen) with an epitaxial relationship to the alloy substrate. Yet the oxide is very fine-grained. The orientations are such that the densest packed directions are parallel to each other

$$[1\,1\,0]_{\mathrm{Alloy}} \parallel [1\,1\,0]_{\mathrm{NiCr_2O_4}} \parallel [1\,0\,0]_{\mathrm{Cr_2O_3}}$$

and

$$[1\,1\,0]_{\mathrm{Alloy}} \parallel [1\,1\,0]_{\mathrm{NiO}}$$

On unimplanted alloy the oxide nuclei have random orientation.

In summary, implanted yttrium affects oxide growth from the very beginning when it promotes the formation of chromium-rich oxide nuclei. After a longer time its effect is enhancement of the chromium content in the inner oxide layer. Yttrium remains concentrated in the inner oxide layer where it blocks outward cation diffusion and thereby slows oxide growth. Yttrium also prevents porosity in the inner oxide layer and makes it adhere better to the alloy.

Acknowledgements

This research was supported by the NSF Materials Research Laboratory at CWRU. One of us (CHY) acknowledges TRW Inc. for a Fellowship. The HVEM and RBS work were performed at Argonne National Laboratory with the kind assistance of E. A. Ryan and R. S. Averback, respectively. M. J. Bennett, UK Atomic Energy Authority, is thanked for many useful discussions.

References

1. J. K. ANTILL and K. J. PEAKALL, *J. Iron Steel Inst.* **205** (1967) 1136.
2. J. STRINGER, B. A. WILCOX and R. L. JAFFEE, *Oxid. Metals* **5** (1972) 11.
3. F. H. STOTT, J. S. PUNNI, G. C. WOOD and G. DEARNALEY, "Ion Implantation into Metals", edited by V. Ashworth, W. A. Grant and R. P. M. Proctor (Pergamon, London, 1982) p. 245.
4. J. J. BENNETT, B. A. BELLAMY, G. DEARNALEY and M. R. HOULTON, "International Congress on Metallic Corrosion Proceedings", Vol. 2 (National Research Council of Canada, Ottawa, 1984) p. 416.
5. C. H. YANG, P. A. LABUN, G. WELSCH, T. E. MITCHELL and M. J. BENNETT, *J. Mater. Sci.* **22** (1987) 449.
6. C. H. YANG, G. WELSCH and T. E. MITCHELL, *Mater. Sci. Engng.* **69** (1985) 351.
7. M. J. BENNETT, H. E. BISHOP, P. R. CHALKER and A. T. TUSON, *ibid.* **90** (1987) 177.
8. H. M. FLOWER and B. A. WILCOX, *Corros. Sci.* **17** (1977) 253.
9. R. S. AVERBACK, *Mater. Sci. Forum* **2** (1984) 99.
10. W. K. CHU, J. W. MAYER, M. A. NICOLET, T. M. BUCK, G. AMSEL and F. EISEN, *Thin Solid Films* **17** (1973) 1.
11. L. W. HOBBS, H. T. SAWKILL and M. T. TINKER, "High Temperature Corrosion of Metals and Alloys" (Japan Institute of Metals, Tokyo, 1983) p. 115.
12. V. R. HOWES, *Corrosion Sci.* **7** (1967) 735.
13. M. G. C. COX, B. McENANEY and V. D. SCOTT, *Phil. Mag.* **29** (1974) 585.
14. I. MANNING, cited by G. K. Hubler, "Ion Beam Processing", NRL Memo Report5928 (1987).
15. J. C. PIVIN, C. ROQUES-CARMES, J. CHAUMONT and H. BERNAS, *Corros. Sci.* **20** (1980) 947.
16. W. E. KING, M. L. PETERSON and J. F. REDDY, *J. Physique* **C4** (1985) 423.
17. M. J. BENNETT, J. A. DESPORT, M. R. HOULTON, P. A. LABUN and J. M. TITCHMARSH, AERE-13107 April (1988).
18. P. A. LABUN, PhD thesis, Case Western Reserve University (1982).
19. M. J. FLEETWOOD, *J. Inst. Metals* **94** (1966) 218.
20. M. S. SELTZER, B. A. WILCOX and J. STRINGER, *Metall. Trans.* **3** (1972) 2391.
21. M. S. SELTZER and B. A. WILCOX, *ibid.* **3** (1972) 2357.
22. J. F. LAURENT and J. BENARD, *Compt. Rend.* **241** (1955) 1204.
23. K. HOSHINO and N. L. PETERSON, *J. Amer. Ceram. Soc.* **66** (1983) C-202.
24. D. P. MOON and M. J. BENNETT, Personal communication (1987).

25. B. BENDER, D. B. WILLIAMS and M. R. NOTIS, *J. Amer. Ceram. Soc.* **63** (1980) 542.
26. P. KOFSTAD and K. P. LILLERUD, *J. Electrochem. Soc.* **127** (1980) 2410.
27. H. T. MICHELS, *Metal. Trans.* **7A** (1976) 379.
28. H. NAGAI, T. FUJIKAWA and K. SHOKI, *Trans. Jpn. Inst. Metals* **24** (1983) 581.
29. F. A. GOLIGHTLY, F. H. SCOTT and G. C. WOOD, *Oxid. Metals* **10** (1979) 163.
30. A. B. ANDERSON, S. P. MEHANDRU and J. SMIALEK, *J. Electrochem. Soc.* **132** (1985) 1695.

Received 22 December 1988
and accepted 23 August 1989